IOP Publishing Journal of Micromechanics and Microengineering

J. Micromech. Microeng. **17** (2007) 1281–1288 doi:10.1088/0960-1317/17/7/010

Vision-based cellular force measurement using an elastic microfabricated device

Xinyu Liu, Yu Sun, Wenhui Wang and Bob M Lansdorp

Advanced Micro and Nanosystems Laboratory, University of Toronto, 5 King's College Road, Toronto, Ontario M5S 3G8, Canada

E-mail: sun@mie.utoronto.ca

Received 12 March 2007, in final form 14 May 2007
Published 5 June 2007
Online at stacks.iop.org/JMM/17/1281

Abstract

Manipulation and characterization of individual biological cells require cellular forces to be precisely measured in real time. This paper presents a computer vision-based cellular force measurement platform that allows for the use of a single vision sensor (CCD/CMOS camera) to simultaneously obtain two forms of feedback (i.e., vision and force). A novel silicone elastomer-based cell holding device and a sub-pixel visual tracking algorithm are developed. Deflections of elastic, low-stiffness structures are visually tracked, and material deflections are subsequently transformed into cellular forces. Experimental results demonstrate that the current vision-based force sensing system is capable of performing robust cellular force measurements at a full 30 Hz with a 3.7 μN resolution. Importantly, the vision-based cellular force sensing framework established in this study is not scale- or cell-line-dependent. The device design, visual tracking algorithm, and experimental technique form a powerful framework that would permit visually resolving cellular forces in real time with a sub-nanoNewton (26 pN) resolution for applications in single cell manipulation and characterization.

(Some figures in this article are in colour only in the electronic version)

1. Introduction

Mechanical force plays a critical role in the interactions of biological cells with their surrounding environment. In order to understand how mechanical interactions affect the function of biological cells, cellular forces must be quantitated and their effects on the function and morphology of cells should be studied [1]. The capability of precisely measuring small forces at the microscale is also important for providing force feedback during microrobotic biomanipulation where biological cells being handled can be easily damaged [2].

Force measurements at the micro–nanoscale are often conducted using MEMS (microelectromechanical systems) transducers such as capacitive force sensors [1, 3] and piezoresistive cantilevers [4, 5]. Compared to other cellular force measurement techniques, such as optical tweezers [6], atomic force microscopy (AFM) [7], magnetic bead measurement [8] and micropipette aspiration [9], MEMS force sensors are more cost-effective and provide flexibility for system integration. However, the construction of MEMS force transducers typically depends on silicon micromachining that requires sophisticated equipment sets and much processing effort. Significant care must also be taken in properly designing and shielding electronic detection circuits in order to obtain a satisfactory force measurement resolution. Furthermore, issues such as biocompatibility and operating in an aqueous environment for biological cells to survive often pose stringent challenges and intricacies in MEMS design, material selection, and microfabrication.

As microrobotic biomanipulation and single cell mechanical characterization in cellular biomechanics are universally conducted under an optical microscope that provides high-resolution, low depth-of-field visual feedback, it is highly desirable to simultaneously obtain high-resolution force measurements extracted from visual feedback. Thus, no distinct sensing modalities are required and a single vision sensor (CCD/CMOS camera) is capable of providing two forms of feedback (i.e., vision and force) [10, 11]. For cellular force sensing, this concept can be implemented by visually tracking flexible structural deformations and,

 © 2007 IOP Publishing Ltd Printed in the UK

subsequently, transforming material deformations into forces.

It has been over two decades since the flexible substrate method was introduced for characterizing mechanical interactions between biological cells and their surrounding environment [12]. A flexible thin substrate using silicone or polyacrylamide is used as a cellular traction force sensor [13–18]. Local deformations caused by adherent cells indicate the distribution of traction forces. In order to visually track the local deformation, fluorescent microbeads are usually distributed in the substrate as tracking markers, the displacements of which can be directly measured by fluorescent microscopy [14, 15]. The discrete local deformation, described by the displacements of the microbeads, is interpolated to determine the deformation distribution of the whole substrate. The continuous substrate deformation is finally converted into the distribution of traction forces using various semi-infinite-space elasticity models [16, 17], in which complex calculations are necessarily involved. It was demonstrated that such semi-infinite-space elasticity models are highly sensitive to the noise in the deformation data [18], and therefore require the introduction of additional information such as localization and smoothness assumption.

Instead of using flexible thin substrates, an innovative approach employing microfabricated PDMS (polydimethylsiloxane) post/pillar structures as force transducers was recently reported to visually measure traction forces generated by adherent cells (smooth muscle cells [19], epithelial cells [20], and cardiac myocytes [21]). Unlike the flexible thin substrates, the post/pillar structures do not require heavily complex computations for calculating traction forces. Compared to silicon-based MEMS devices, PDMS-based devices are biocompatible and can be readily constructed using the soft lithography technique [22, 23] without requiring intensive microfabrication efforts or sophisticated equipment sets. In [19, 21], off-line image post-processing was conducted to measure PDMS structural deflections. Despite the low computation complexity and ease of fabrication, the cellular force measurement accuracy in these studies [19–21] was not warranted because the small-deflection assumption in linear elasticity was not satisfied and the shear component of deflected posts was not considered. Additionally, without adopting sub-pixel visual feature tracking techniques, the force measurement resolution was sacrificed.

Although the flexible thin substrate method [12–18] and the post/pillar approach [19–21] can be applied to measuring how much forces are generated by adherent cells at adhesion sites, they do not allow for studying how externally applied forces affect cell responses, which is particularly relevant to suspended cells. A range of applications call for a new experimental platform, such as autonomous force-controlled microrobotic cell injection (e.g., injecting foreign materials into individual cells to treat severe male infertility or to create transgenic organisms for cancer studies [2]) and cell indentation for mechanical property characterization in which forces applied by a micropipette or indenter to a single cell must be precisely measured in real time.

This paper presents a PDMS cell holding device and a sub-pixel visual tracking algorithm used together to visually quantify applied forces to a single cell. The applied forces are transmitted to low-stiffness, protruding posts located inside a cavity, as illustrated in figure 1. The device, visual tracking algorithm, and experimental technique form a powerful framework for visually resolving cellular forces in real time with a high resolution during microrobotic cell manipulation or cell indentation for single cell biomechanical studies.

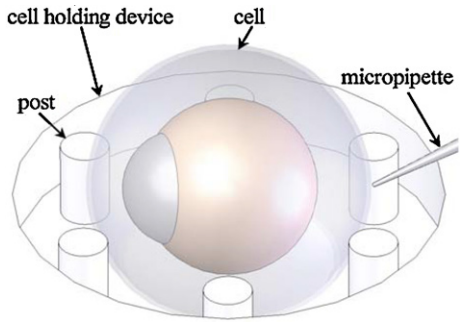

Figure 1. Schematic configuration of vision-based cellular force measurement.

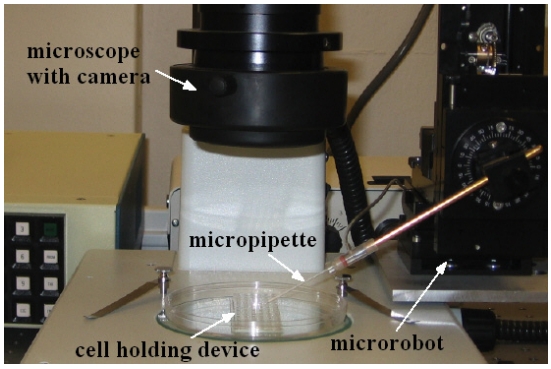

Figure 2. Microrobotic cell manipulation system used to conduct vision-based cellular force measurements.

2. System setup

2.1. Microrobotic cell manipulation system

The system, shown in figure 2, consists of a PDMS cell holding device, an optical microscope with a CMOS camera and a three-degrees-of-freedom microrobot with a 40 nm positioning resolution along each axis. The microrobot controls the motion of an injection micropipette to apply force to a biological cell that is surrounded by low-stiffness protruding posts inside a cavity. Although only a single element is shown in figure 3(*b*), there are arrays of such elements on the PDMS cell holding device. The system setup is mounted on a vibration isolation table for minimizing vibration-induced vision/force measurement errors.

2.2. PDMS cell holding device

The PDMS cell holding device (figure 3(*b*)) was constructed using replica-molding process (figure 3(*a*)). Because processing conditions determine Young's modulus and

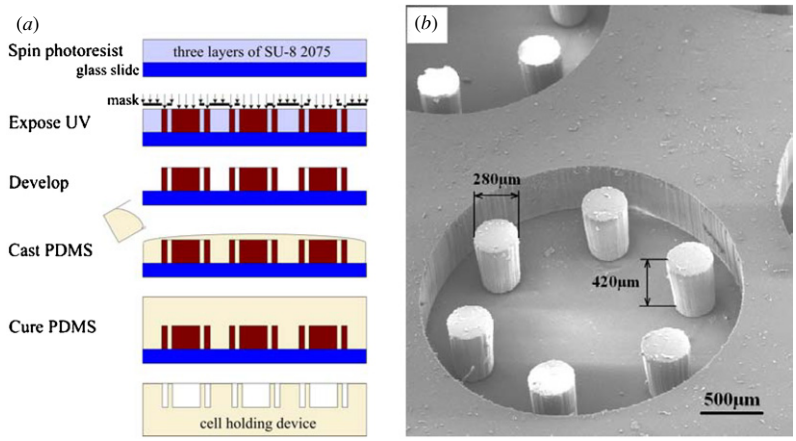

Figure 3. Fabrication of the PDMS cell holding device. (*a*) Schematic drawing of replica-molding process. (*b*) Scanning electron microscope (SEM) image of the cell holding device.

structural stiffness that affect the accuracy of force measurements, the fabrication details are described herein.

Photolithography was conducted using three layers of SU-8 2075 (MicroChem, USA) spin-coated on a glass slide at 1400 rpm for each layer. Each SU-8 layer was pre-baked at 65 °C for 10 min and 95 °C for 70 min. The SU-8 layers were exposed by 365 nm UV light (31 mJ cm^{-2}) for 25 s, post-exposure baked at 65 °C for 1 min and 95 °C for 10 min and finally developed for 120 min. PDMS was prepared by mixing Sylgard 184 (Dow Corning, USA) and curing agent with a weight ratio of 10:1, and then degassed in a vacuum chamber to eliminate air bubbles. The SU-8 template was then immersed into the PDMS pre-polymer. After a second-time degassing and curing at 75 °C for 8 h, the PDMS cell holding device was peeled off the SU-8 template. The depth of the cavity and protruding posts is 420 μm, and the diameter of the posts is 280 μm (figure 3(*b*)). In order to make the PDMS surface hydrophilic, the devices were treated in an oxygen plasma cleaner (Harrick Scientific, USA) for 40 s before use.

3. Vision-based cellular force measurement

3.1. Zebrafish embryo preparation

The zebrafish has emerged as an important model organism for the development and genetic studies, due to the similarities in gene structures to the human being, external fertilization and development, short development period, and the transparency of embryos making it easy to observe the fate of individual cells throughout developmental stages. Additionally, the large size of zebrafish embryos (∼1.2 mm including chorion that is the outside membrane in figure 4) makes the handling and manipulation of these cells less demanding. Although zebrafish embryos were chosen in this study to demonstrate vision-based cellular force sensing, the PDMS cell holding device can be readily scaled down for studying cells of smaller sizes (e.g., mouse embryos), and the methodology presented in the rest of this paper is not scale- or cell-type-dependent. Zebrafish embryos at 50%-epiboly stage were collected in accordance with the established standard procedure [24]. The experiments were conducted at room temperature of 23 °C.

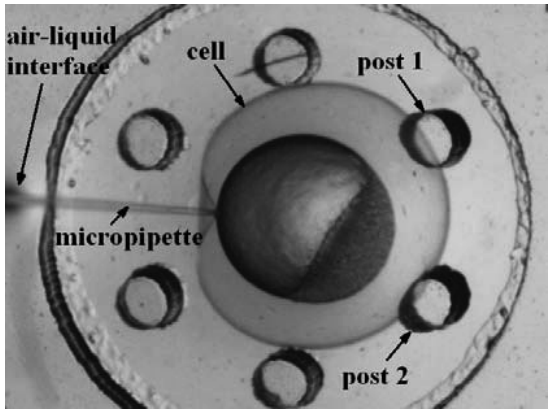

Figure 4. Indentation forces applied by the micropipette cause the two supporting posts to deflect.

3.2. Force analysis

Figure 4 shows an image captured in the cell indentation experiments. An injection micropipette mounted on the microrobot is employed to exert an indentation force to a zebrafish embryo, which deflects the two supporting posts against the cell. If the number of supporting posts were increased in the device, the applied force would be distributed among more supporting posts, leading to a decreased force sensitivity and lower measurement bandwidth. In experiments, the micropipette tip, cell holding device and cell are all immerged into culture medium. The shades of non-supporting posts are due to optical distortions caused by the culture medium. Post deflections, measured by a visual tracking algorithm that is discussed in following sub-sections, are fitted to an analytical mechanics model to obtain contact forces between the cell and posts. Based on the contact forces, the injection/indentation force applied by the micropipette is obtained through a force analysis.

In the experimental configuration, the radius of the cell (600 μm) is larger than the depth of the cavity/posts (420 μm), resulting in a point contact between the cell and supporting posts before post deflections occur. Throughout indentation, the cell deformation in the proximity of cell–post contact areas

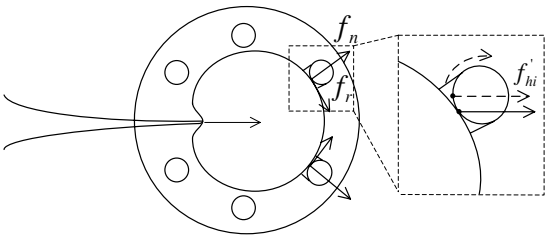

Figure 5. Cell indentation and force analysis.

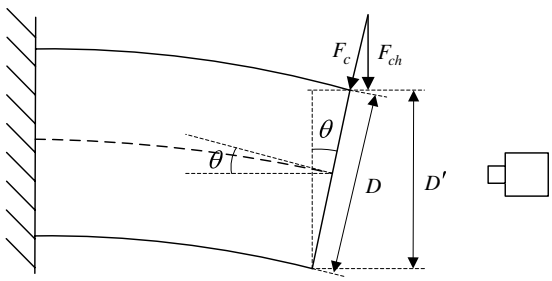

Figure 6. Post deflection slope measurement.

was not noticeable. The micropipette tip mounted on the microrobot is adjusted and well aligned to achieve symmetrical loading. Thus, cell–post contact forces can be considered as concentrated loads as shown in figure 5.

In order to guarantee a valid application of linear elasticity that requires small structural deflections, the slope of the posts' free ends was measured. The slope, θ, shown in figure 6 is

$$\theta = \cos^{-1}\left(\frac{D'}{D}\right), \tag{1}$$

where D is the post diameter, and D' is the projection of the deflected post which was measured from image sequences. The maximum value of θ was found to be 13.7°, which satisfies $\sin\theta \approx \theta$ and thus, the small-deflection assumption of linear elasticity holds [25]. It also indicates that the contact force between the cell and posts (F_c in figure 6) can be approximated by the horizontal components F_{ch}, because $\cos\theta \approx 1$ holds throughout the deflection process. The small vertical force component and hydrostatic pressure exerted by the fluidic environment are at least three orders of magnitude lower than sufficient for buckling a supporting post.

Figure 5 shows that the contact forces between the cell and posts are composed of a normal force f_n and a frictional force f_r. The cell is treated as elastic during injection/indentation due to the fact that continuous loading in practice does not leave sufficient time for cellular creep or relaxation to occur. Thus, the injection/indentation force F is balanced by the horizontal components f_{hi} of the two contact forces:

$$F = \sum_{i=1}^{2} f_{hi}. \tag{2}$$

For both supporting posts, the horizontal force component f_{hi} can be decomposed into an equal force f'_{hi} crossing the post center plus a torque T_{hi}. The torque does not produce post deflection, and only f'_{hi} causes horizontal deflections of the supporting posts. Therefore, f'_{hi} can be obtained by feeding horizontal deflections of the posts into the posts' mechanics

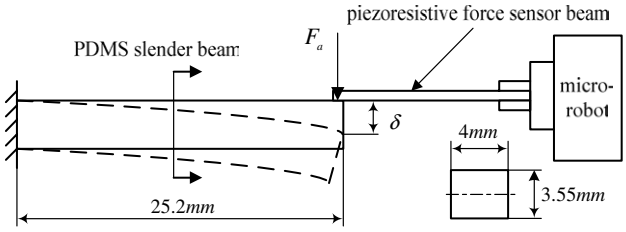

Figure 7. System setup for PDMS modulus calibration.

model. The ratio of post height (420 μm) to diameter (280 μm) in this design does not satisfy the pure bending assumption of linear elastic beams (i.e., height to diameter ratio must be greater than 5); thus, both bending and shearing must be considered in order to map the deflection to the applied force [25]:

$$f'_{hi} = \frac{\delta_{hi}}{\frac{H^3}{3EI} + \frac{20(1+\gamma)H}{9AE}}, \tag{3}$$

where $i = 1, 2$, δ_{hi} is the horizontal deflection, H and A are the post height and cross-sectional area, I is the moment of inertia, and E and γ are the Young's modulus and Poisson's ratio (for PDMS, the Poisson's ratio is 0.5 [26]). Note that drag forces applied to the supporting posts by the fluidic environment were safely ignored, which were determined to be at a force level of 10^{-13} N using the fluidic drag model [27].

Post diameters are considered uniform along the height, which was verified by high-magnification SEM imaging. Consequently, the moment of inertia of each post can be expressed as

$$I = \frac{\pi D^4}{64}. \tag{4}$$

Combining equations (2)–(4) yields

$$F = \sum_{i=1}^{2} \frac{\delta_{hi}}{\frac{64H^3}{3\pi ED^4} + \frac{20(1+\gamma)H}{9AE}}. \tag{5}$$

In equation (5), the only unknown parameters are Young's modulus E, and post-horizontal deflections δ_{hi}. For PDMS, it is known that different processing conditions result in large variations of Young's modulus values [28]. In order to accurately determine the Young's modulus value of the constructed PDMS posts, calibration experiments were conducted.

3.3. Calibration of Young's modulus

To determine the Young's modulus value, a PDMS cantilever beam produced under the same processing conditions was calibrated with a piezoresistive silicon force sensor (AE801, SensorOne, USA). It has been demonstrated that Young's modulus characterized from bulk PDMS and a micro-PDMS structure, both constructed with the same microfabrication parameters, differs within 5% [29].

As shown in figure 7, the sensor was controlled to push the free end of the PDMS cantilever beam. In the calibration experiment, the contact area was carefully controlled such that the loads applied to the PDMS cantilever beam can be treated as concentrated forces. The stiffness of the silicon force sensor is 2 N mm^{-1}, from which deflections of the

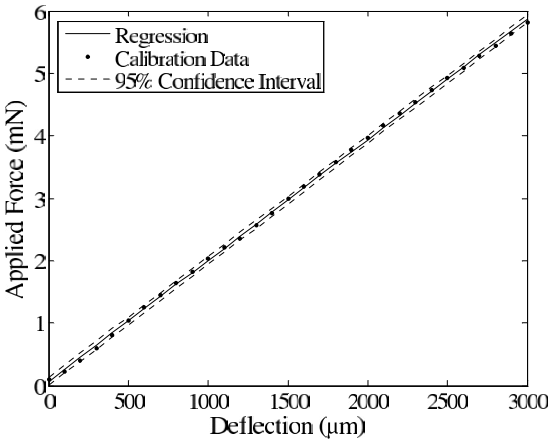

Figure 8. Calibration results of the PDMS cantilever beam.

sensor beam were calculated. The deflection of the PDMS cantilever beam is thus equivalent to the difference between the displacement of the microrobot and the deflection of the sensor beam. The calibration data shown in figure 8 were substituted into the following mechanics model describing pure-bending cantilever beams [25]:

$$F_a = \frac{3EI}{H^3}\delta, \tag{6}$$

where F_a and δ are the applied force and the free-end deflection of the PDMS cantilever beam. The Young's modulus value was determined to be 707.2 kPa, which is within the previously reported range [28].

3.4. Real-time sub-pixel visual tracking of post deflections

In order to accurately track post deflections, a sub-pixel visual tracking algorithm is developed. The task is two fold, to track image patches of the top surfaces of supporting posts as well as to accurately detect the circular center positions. Gradient-based tracking algorithms such as optical flow [30] are not capable of providing robust tracking performance. This is because gradient-based algorithms assume pixel intensities translated from one frame to the next remain constant (i.e., the brightness constancy assumption). However, shadows resulting from post deflections render this assumption invalid.

In this study, a template matching algorithm with template update is used to track the motion of the supporting posts, providing processing areas for the subsequent least-squares circle detection (LSCD) to determine posts' center positions. Template matching with constant template update permits small changes in image patterns between successive frames of images; therefore, it is capable of robustly tracking the top surfaces of the two supporting posts. Accumulative errors caused by updating templates are eliminated in the subsequent detection of circular centers using the LSCD algorithm.

Pixel intensity in an image can be represented by $I_n(\mathbf{x})$, where $\mathbf{x} = (x, y)^{\mathrm{T}}$ is the pixel position in the image coordinate frame, and $n = 0, 1, 2, \ldots$ is the image frame number. Initially, a square patch (i.e., the initial template) of 90 × 90 pixels, containing the post top surface, is acquired for each of the two supporting posts. The initial template is denoted by $T_0(\mathbf{x}_T)$, where $\mathbf{x}_T = (x_T, y_T)^{\mathrm{T}}$ is the pixel position in the template coordinate frame. Then, the template used in the nth frame is $T_n(\mathbf{x}_T)$. Within each frame of image, the sum-of-squared-differences (SSD) correlation measure is calculated to locate the best match within a search window of 140 × 140 pixels. The displacement of the tracking target in the nth frame of image, $\Delta\mathbf{x}_n = (\Delta x, \Delta y)^{\mathrm{T}}$, can be obtained by computing

$$\Delta\mathbf{x}_n = \arg\min_{\Delta\mathbf{x}} \sum_{\mathbf{x}_T \in T_n} [I_n(\mathbf{x}_n + \mathbf{x}_T + \Delta\mathbf{x}) - T_n(\mathbf{x}_T)]^2, \tag{7}$$

where $\mathbf{x}_n$ is the template position in the coordinate frame of the nth image. The template is updated after each template matching operation by selecting the current best match

$$T_{n+1}(\mathbf{x}_T) = I_n(\mathbf{x}_n + \mathbf{x}_T + \Delta\mathbf{x}_n). \tag{8}$$

The time complexity of the algorithm depends on sizes of the template and search window. In this study, the template size is determined by the area of post top surfaces. A large enough search window was chosen to handle larger displacements, provided that images can be processed in real time (30 Hz) including image patch tracking and circular center detection.

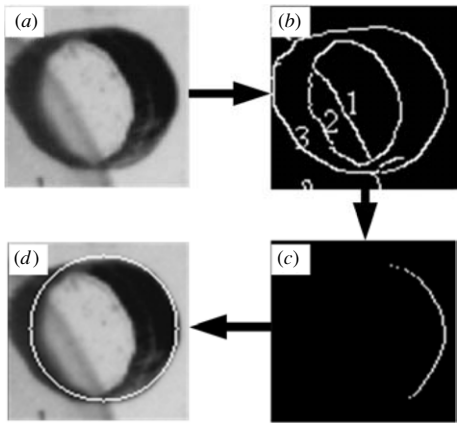

Figure 9. Circular center detection of a post top surface. (*a*) Original image patch. (*b*) Resulting image patch after Canny edge detection. (*c*) Rightmost portion of the circle used for circle fitting. (*d*) Final fitted circle.

After tracking the image patches that contain post top surfaces, the circular center positions are detected by the LSCD algorithm. Canny edge detection of a tracked image patch (figure 9(*a*)) results in an edge image (figure 9(*b*)). The curve edge of post top surface is then extracted for circle fitting. During curve edge extraction, only the rightmost portion of the circle (figure 9(*c*)) was selected for circle fitting. The selection criterion is to minimize the error in the circle detection process. The left-half (edge 2 in figure 9(*b*)) was discarded as it is distorted and blurred due to the fact that the view was blocked by a portion of the cell membrane (edge 1 in figure 9(*b*)), which can cause significant errors in circle fitting. Edge 3 is the shadow contour that was also discarded.

The extracted curve edge points were then fitted to a circle using a least-squares fitting algorithm. Denote the coordinates of edge points as (x_i, y_i), $i = 0, 1, 2, \ldots, n$. The circle fitting algorithm minimizes the sum of squares of algebraic distance

$$O(a, b, R) = \sum_{i=1}^{n} [(x_i - a)^2 + (y_i - b)^2 - R^2]^2, \tag{9}$$

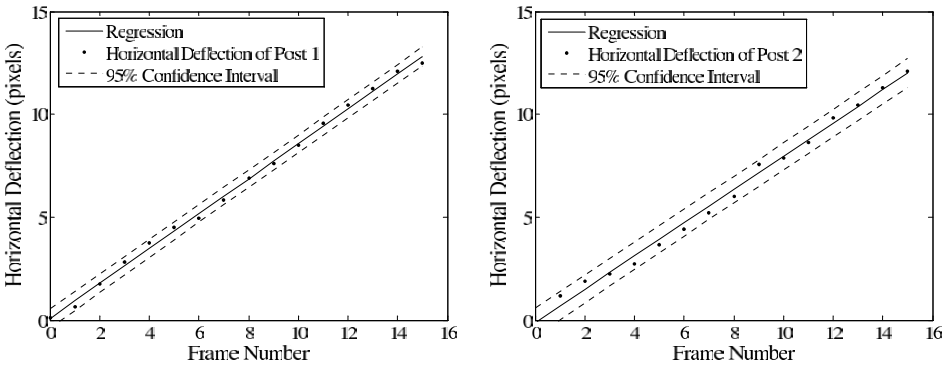

Figure 10. Visual tracking results of horizontal deflections of post 1 (left) and post 2 (right).

Table 1. Vision-based cellular force measurement resolution.

Objective magnification	NA	Rayleigh limit (μm)	Pixel size (μm)	Deflection resolution (pixel)	Force resolution (μN)
2.5×	0.07	3.93	4.17	0.45	12.7
4×	0.13	2.12	2.27	0.58	8.9
6.4×	0.13	2.12	1.56	0.40	4.2
10×	0.30	0.92	1.00	0.54	3.7

where a and b are the coordinates of the circle center and R is the circle radius. Rewriting equation (9) yields an objective function

$$O(A, B, C) = \sum_{i=1}^{n} (z_i + Ax_i + By_i + C)^2 \qquad (10)$$

where $z_i = x_i^2 + y_i^2$, $A = -2a$, $B = -2b$, and $C = a^2 + b^2 - R^2$. Differentiating equation (10) with respect to B, C and D produces a linear equation set, from which the center coordinates and radius of the circle are obtained.

4. Experimental results and discussion

Figure 4 was taken with a 2.5× objective (NA 0.07) in order to have both the cell and supporting posts inside the field of view. The calibrated pixel size is 4.17 μm × 4.17 μm. The micropipette used for indenting cells has an outside diameter of 25 μm at the tip end. The indentation speed was controlled at 600 μm s^{-1}.

Images were captured at 30 fps. The template matching algorithm and the LSCD algorithm together cost 22.3 ms for processing each frame of image, proving the real-time capability of the vision-based force sensing system. Visual tracking results of the two supporting posts (post 1 and post 2 in figure 4) are shown in figure 10. The tracking resolution is 0.45 pixel for post 1 and 0.67 pixel for post 2. The mechanical stiffness of each post is 6.76 μN μm^{-1}.

The visually measured horizontal deflection results were substituted into the post-mechanics model (equation (5)) to calculate indentation forces corresponding to each frame of image. The cellular deformation on the micropipette side was obtained by subtracting the average horizontal deflections of the two posts from the micropipette's displacement (i.e., displacement of the microrobot). Figure 11 shows the visually resolved indentation forces and corresponding cellular deformation. Under the 2.5× objective with NA 0.07, the vision-based force measurement resolution is 12.7 μN.

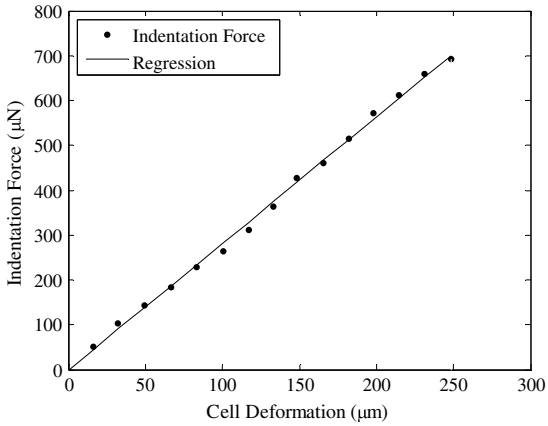

Figure 11. Force–deformation curve of indented zebrafish embryo.

Experimental results demonstrate that the vision-based force sensing system is capable of performing robust force measurements at a full 30 Hz. The force measurement resolution depends on optical conditions and is greatly improved with objectives of higher magnifications. As shown in table 1, with a 10× objective (NA 0.3), the system is capable of visually resolving forces down to 3.7 μN.

Possible insignificant error sources of the vision-based cellular force measurements, which were not taken into account in this study, include (1) the assumption that the supporting posts are perfectly uniform along the post height, (2) the assumption that contact forces between the cell and posts are purely in-plane, concentrated loads, (3) the fact that drag forces applied to the supporting posts by the fluidic environment are not significant for consideration, and (4) negligible device substrate deformations determined by finite element simulation to be smaller than 1.53 nm.

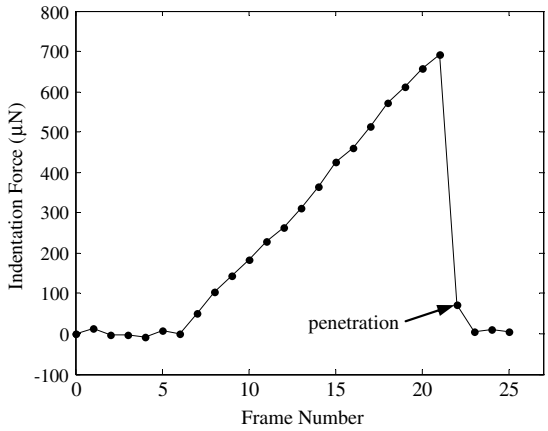

Figure 12. Experimental data for visually detecting the penetration of the cell membrane during microrobotic cell injection.

Besides the applicability to cellular biomechanics, the device and tracking algorithm can provide important force feedback in microrobotic cell injection. The cell membrane penetration can be precisely determined from the vision-based force measurement results for subsequent material deposition (figure 12). The abrupt position change of the supporting posts signals cell membrane penetration. Forces required to penetrate the outside membrane (*chorion*) were determined to be 692.8 μN, in satisfactory agreement with previous measurement results using a piezoelectric sensor for investigating protein structure development of the chorion of zebrafish embryos [31].

Importantly, the vision-based cellular force sensing framework established in this study is not scale-dependent. Compared to zebrafish embryos, the majority of suspended cell lines have a much smaller size (e.g., mouse embryos are 60 μm in diameter). The presented PDMS cell holding device that was constructed using soft lithography can be scaled down to accommodate cells of smaller sizes. Soft lithography permits the construction of PDMS structures with an aspect ratio up to 10:1 (post height versus post diameter) via process optimization. For example, a cell holding device with supporting posts of 25 μm in height and 5 μm in diameter (aspect ratio: 5:1; mechanical stiffness of each post: 4 nN μm^{-1}), based on a 0.5 pixel visual tracking resolution obtained in this study, has the capability of visually resolving forces down to 0.52 nN with a 40$\times$ objective.

With an aspect ratio of 10:1, a cell holding device with supporting posts of 20 μm in height and 2 μm in diameter (mechanical stiffness of each post: 0.2 nN μm^{-1}) would have the capability of visually resolving forces down to 26 pN. Although drag forces applied to these scaled-down posts by the fluidic environment are still safe to ignore (10^{-19} N determined with the fluidic drag model [27]), several other issues might appear significant and must be taken into account when resolving forces at the pN level. Finite strain conditions must be strictly satisfied in order to guarantee that PDMS exhibits nearly ideal elastic properties [32]. Due to the temperature dependence of PDMS modulus (1.1 kPa $^\circ$C^{-1}) [33], constancy of temperature needs to be maintained during experiments. Shape defects from microfabrication imperfectness would also be important to consider in force analysis and mechanics modeling.

5. Conclusion

This paper presented a method to robustly measure forces applied to single biological cells through the use of a microfabricated PDMS device and a sub-pixel computer vision tracking algorithm with a resolution of 0.5 pixel. The Young's modulus value of the PDMS device was experimentally calibrated to be 707.2 kPa. Based on visually tracked deflections of elastic, low-stiffness supporting posts, the quantitative force measurement results on zebrafish embryos were obtained through an analytical mechanics model. Experimental results demonstrate that the system is capable of performing robust cellular force measurements at a full 30 Hz with a 3.7 μN resolution. A realistic estimate reveals that the methodology presented in this paper is capable of resolving forces down to 26 pN with a scaled-down cell holding device (supporting posts of 20 μm in height and 2 μm in diameter). The device design, visual tracking algorithm, and experimental technique provide an extremely cost-effective, yet powerful experimental platform for investigating the mechanical properties of many cell types of different sizes and for providing real-time cellular force feedback during automated microrobotic cell manipulation.

Acknowledgment

This research was supported by the Natural Sciences and Engineering Research Council of Canada (NSERC).

References

[1] Sun Y, Wan K T, Nelson B J, Bischof J and Roberts K 2003 Mechanical property characterization of the mouse zona pellucida *IEEE Trans. NanoBioSci.* **2** 279–86

[2] Sun Y and Nelson B J 2002 Biological cell injection using an autonomous microrobotic system *Int. J. Robot. Res.* **21** 861–8

[3] Sun Y, Fry S N, Potassek D P, Bell D J and Nelson B J 2005 Characterizing fruit fly flight behaviour using a microforce sensor with a new comb drive configuration *J. Microelectromech. Syst.* **14** 4–11

[4] Lin G, Palmer R E, Pister K S J and Roos K P 2001 Miniature heart cell force transducer system implemented in MEMS technology *IEEE Trans. Biomed. Eng.* **9** 996–1006

[5] Fauver M E, Dunaway D L, Lillenfeld D H, Craighead H G and Pollack G H 1998 Microfabricated cantilevers for measurement of subcellular and molecular forces *IEEE Trans. Biomed. Eng.* **45** 891–8

[6] Conia J, Edwards B S and Voelkel S 1997 The micro-robotic laboratory: optical trapping and scissing for the biologist *J. Clin. Lab. Anal.* **11** 28–38

[7] Charras G T, Lehenkari P P and Horton M A 2001 Atomic force microscopy can be set to mechanically stimulate osteoblasts and evaluate cellular strain distribution *Ultramicroscopy* **86** 85–95

[8] Fass J N and Odde D J 2003 Tensile force dependent neurite elicitation via Anti-β1 integrin antibody-coated magnetic beads *Biophys. J.* **85** 623–36

[9] Hochmuth R M 2000 Micropipette aspiration of living cells *J. Biomech.* **33** 15–22

[10] Greminger M A and Nelson B J 2004 Vision-based force measurement *IEEE Trans. Pattern Anal. Mach. Intell.* **26** 290–8
[11] Luo Y H and Nelson B J 2001 Fusing force and vision feedback for manipulating deformable objects *J. Robot. Syst.* **18** 103–17
[12] Harris A K, Wild P and Stopak D 1980 Silicone rubber substrata: a new wrinkle in the study of cell locomotion *Science* **208** 177–9
[13] Beningo K A and Wang Y L 2002 Flexible substrata for the detection of cellular traction forces *Trends Cell Biol.* **12** 79–84
[14] Beningo K A, Lo C M and Wang Y L 2002 Flexible polyacrylamide substrates for the analysis of mechanical interactions at cell–substrate adhesions *Methods Cell Biol* **69** 325–39
[15] Rieu J P, Barentin C, Maeda Y and Sawada Y 2005 Direct mechanical force measurements during the migration of Dictyostelium slugs using flexible substrata *Biophys. J.* **89** 3563–76
[16] Dembo M and Wang Y L 1999 Stresses at the cell-to-substrate interface during locomotion of fibroblasts *Biophys. J.* **76** 2307–16
[17] Balaban N Q *et al* 2001 Force and focal adhesion assembly: a close relationship studied using elastic micropatterned substrates *Nat. Cell Biol.* **3** 466–72
[18] Schwarz U S, Balaban N Q, Riveline D, Bershadsky A, Geiger B and Safran S A 2002 Calculation of forces at focal adhesions from elastic substrate data: the effect of localized force and the need for regularization *Biophys. J.* **83** 1380–94
[19] Tan J L, Tien J, Pirone D M, Gary D S, Bhadriraju K and Chen C S 2003 Cells lying on a bed of microneedles: an approach to isolate mechanical force *Proc. Natl Acad. Sci. USA* **100** 1484–9
[20] Roure O D, Saez A, Buguin A, Austin R H, Chavrier P, Siberzan P and Ladoux B 2005 Force mapping in epithelial cell migration *Proc. Natl Acad. Sci. USA* **102** 2390–5
[21] Zhao Y and Zhang X 2006 Cellular mechanics study in cardiac myocytes using PDMS pillars array *Sensors Actuators* A **125** 398–404
[22] Xia Y, Kim E, Zhao X M, Rogers J A, Prentiss M and Whitesides G M 1996 Complex optical surfaces formed by replica molding against elastomeric masters *Science* **273** 347–9
[23] Kim E, Xia Y and Whitesides G M 1995 Polymer microstructures formed by moulding in capillaries *Nature* **376** 581–4
[24] Westerfield M 2000 *The Zebrafish Book: A Guide for the Laboratory Use of Zebrafish* (Eugene, OR: University of Oregon Press)
[25] Ugural A C and Fenster S K 2003 *Advanced Strength and Applied Elasticity* (NJ: Prentice-Hall)
[26] Mark J E *Polymer Data Handbook* (Oxford: Oxford University Press)
[27] Hughes W F and Brighton J A 1999 *Schaum's Outline of Theory and Problems of Fluid Dynamics* (New York: McGraw-Hill)
[28] Armani D, Liu C and Aluru N 1999 Re-configurable fluid circuits by PDMS elastomer micromachining *Proc. IEEE MEMS* pp 222–7
[29] Zhao Y, Lim C C, Sawyer D B, Liao R and Zhang X 2006 Microchip for subcellular mechanics study in living cells *Sensors Actuators* B **114** 1108–15
[30] Horn B K P and Schunk B G 1981 Determining optical flow *Artif. Intell.* **17** 185–203
[31] Kim D H, Hwang C N, Sun Y, Lee S H, Kim B K and Nelson B J 2006 Mechanically characterizing modifications of the zebrafish embryo chorion during early development *IEEE Trans. NanoBioSci.* **5** 89–94
[32] Gupta S, Carrillo F, Li C, Pruitt L and Puttlitz C 2007 Adhesive forces significantly affect elastic modulus determination of soft polymeric materials in nanoindentation *Mater. Lett.* **61** 448–51
[33] Lotters J C, Olthuis W, Veltink P H and Bergveld P 1997 The mechanical properties of the rubber elastic polymer plydimethylsiloxane for sensor applications *J. Micromech. Microeng.* **7** 145–7